Monthly Notices
of the
ROYAL ASTRONOMICAL SOCIETY
MNRAS **444,** 1119–1124 (2014) doi:10.1093/mnras/stu1361

Coronal wave associated with a non-radial filament eruption observed by the *Solar Dynamics Observatory*

R. Zheng,[1,2]★ Y. Jiang,[2] J. Yang[2] and R. Erdélyi[1]

[1]*Solar Physics and Space Plasma Research Center, University of Sheffield, Hounsfield Road, Hicks Building, Sheffield S3 7RH*
[2]*National Astronomical Observatories/Yunnan Astronomical Observatory, Chinese Academy of Sciences, Kunming 650011, China*

Accepted 2014 July 4. Received 2014 July 4; in original form 2014 January 2

ABSTRACT

We analyse a coronal wave that occurred during a non-radial filament eruption observed by the *Solar Dynamics Observatory* on 2011 August 10. The filament underwent an extended time activation phase followed by an abrupt ejection, and during its evolution it rotated towards the south. The eruption was accompanied by fast-wave and slow-perturbation phenomena. The slow perturbation occurred before the eruption and impulsively accelerated almost simultaneously with the eruption; its final propagation velocity was about 300 km s^{-1}, approximately equal tothat of the associated coronal mass ejection. The slow perturbation is possibly an indicator of an expanding loop overlying the filament. The fast wave was probably caused by the rapid inflation of the overlying loop. Because of the eruption location close to the limb and the effect of the complex environment, the fast coronal wave showed different characteristics in different directions: the kick-off speed was about 430–480 km s^{-1}, showing deceleration in some directions, and a high speed of up to 782 ± 21 km s^{-1} in another direction. All the results indicate that the coronal wave was a fast-mode magnetohydrodynamic wave, and the wavelet analysis confirms the periodic wave nature of the coronal wave.

Key words: Sun: activity – Sun: corona – Sun: coronal mass ejections (CMEs).

1 INTRODUCTION

Propagating global coronal waves, often also referred to as extreme ultraviolet (EUV) waves, were originally referred to as 'EIT waves', owing to the fact that they were first observed with the EUV Imaging Telescope (EIT; Delaboudinière et al. 1995) onboard the *Solar and Heliospheric Observatory* (*SOHO*) spacecraft (e.g. Moses et al. 1997; Thompson et al. 1998). Coronal waves usually appear as propagating diffuse bright fronts in EUV images, with phase speeds of several hundred kilometres per second (Thompson & Myers 2009). They generally emanate from flaring and eruptive active regions (ARs). It is now widely accepted that coronal waves are closely associated with coronal mass ejections (CMEs, or other types of mass motions) rather than with solar flares (Biesecker et al. 2002; Cliver et al. 2005; Chen 2006; Zheng et al. 2012).

Coronal waves were generally interpreted as coronal fast-mode magnetohydrodynamic (MHD) waves (e.g. Thompson et al. 1999; Wang 2000; Wu et al. 2001; Ofman & Thompson 2002; Ballai, Erdélyi & Pintér 2005; Long et al. 2008; Gopalswamy et al. 2009; Veronig et al. 2010) that were the coronal counterparts of Hα Moreton waves (Moreton 1960). Because such a fast-mode wave model cannot account for all the observed characteristics of coronal waves, however, several alternative models have been suggested, for example the slow-mode wave (Wills-Davey, DeForest & Stenflo 2007; Wang, Shen & Lin 2009), successive restructuring of the magnetic field (Delannée et al. 2008; Attrill et al. 2007), and field-line stretching (Chen et al. 2002; Zhukov & Auchère 2004; Cohen et al. 2009; Downs et al. 2011; Cheng et al. 2012). For further discussions and reviews, the reader is referred to Wills-Davey & Attrill (2009); Gallagher & Long (2011); Warmuth (2010); Zhukov (2011) and Patsourakos & Vourlidas (2012).

Filament eruptions are frequently associated with other types of solar activity, such as CMEs, flares and/or coronal waves. Understanding the process of filament eruptions is currently a very important topic in solar physics. Regarding the trigger mechanism of filament eruptions, there are two basic models: MHD instability or loss of equilibrium; and tether-cutting reconnection of the leg of the sheared core field (Schmieder, Démoulin & Aulannier 2013). The process of filament eruption often consists of the phases of activation, acceleration, and constant velocity (Sterling & Moore 2004; Koleva et al. 2012). Erupting filaments are sometimes observed to undergo a rotation as they rise, and the filament rotation is commonly interpreted as the conversion of twist into writhe in a kink-instable flux rope (Ji et al. 2003; Green et al. 2007; Bemporad, Mierla & Tripathi 2011; Thompson, Kliem & Török 2012; Yan et al. 2013).

The launch of the *Solar Dynamics Observatory* (*SDO*; Pesnell, Thompson & Chamberlin 2012) enabled coronal waves to be explored in more detail using high-quality data from the Atmospheric

★ E-mail: r.zheng@sheffield.ac.uk

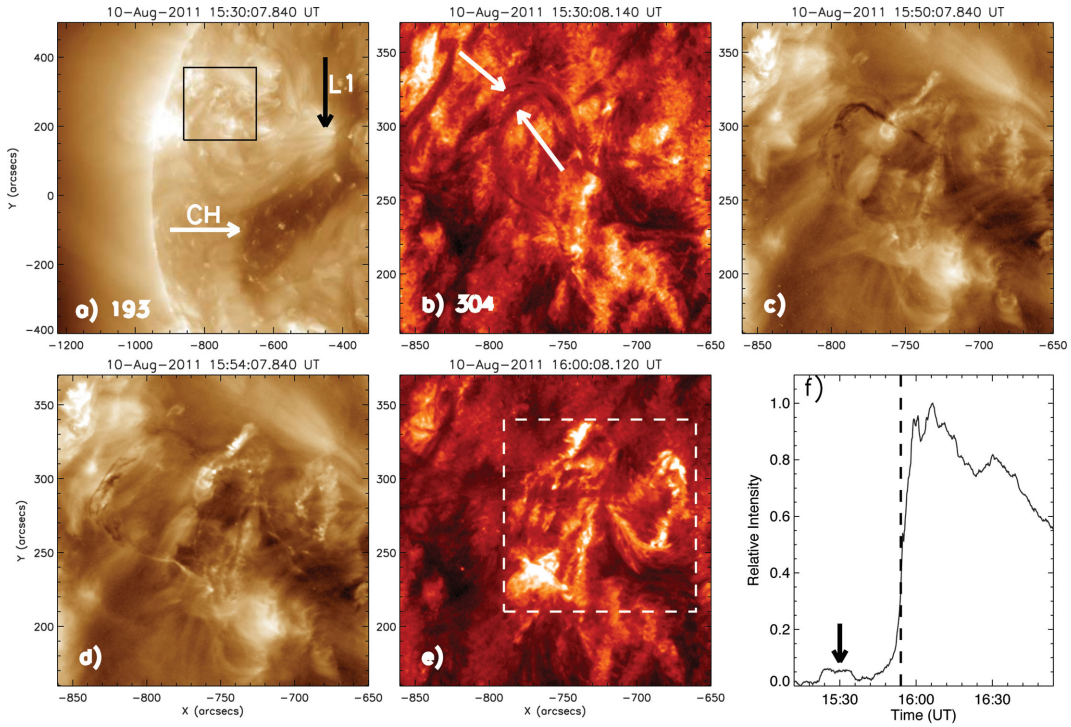

Figure 1. (a) General view of the eruption environment with the original images in AIA 193 Å, and (b–e) evolution of the non-radial filament eruption in AIA 193 and 304 Å. The field of view of the eruption region (b–e) is indicated by the box in (a). Panel (f) shows the light-curve of the flaring region in the box in (e). The white and black arrows in (a) point to the the coronal hole and the footpoint of a large loop overlying the eruption region. The white arrows in (b) indicate the filament. In (f), the arrow and dashed line indicate the brightenings and eruption onset, respectively.

Imaging Assembly (AIA; Lemen et al. 2012) onboard the satellite. These high-cadence and high-sensitivity observations have led to recent discoveries about coronal waves, for example observation of a coronal wave that exhibited multiple fronts and ripples (Liu et al. 2010; Chen & Wu 2011), the existence of the small-scale fast-mode coronal wave (Zheng et al. 2011; Zhang & Liu 2011), the existence of secondary waves triggered in nearby ARs or individual loop-like structures (Li et al. 2012), and wave reflection and transmission through a coronal hole (CH; Olmedo et al. 2012).

In this paper, we focus on the rotation of a coronal wave associated with a non-radial filament eruption on 2011 August 10. The Letter is arranged as follows. Section 2 introduces the observations, the results are reported in Section 3, and the conclusion and discussion follow in Section 4.

2 OBSERVATIONS AND DATA ANALYSIS

On 2011 August 10, a filament was ejected non-radially from the north-east of the solar disc at about 15:50 UT, accompanied by a coronal wave and a CME. Because of the small amount of material emitted at the formation temperature, the image of the filament is faint in Hα filtergrams. Here, we employ primarily data from *SDO*/AIA, combined with observations by the Extreme Ultraviolet Imager (EUVI; Howard et al. 2008) onboard the twin spacecrafts of the *Solar–Terrestrial Relations Observatory* (*STEREO*; Kaiser et al. 2008). The EUV images are between 15:30 and 16:30 UT in AIA 171, 193 and 304 Å and EUVI-B 195 Å. In addition, the CME evolution was well captured by the Large Angle and Spectrometric Coronagraph (LASCO; Brueckner et al. 1995) C2 on the *SOHO* and by the Inner Coronagraph (COR1) on the *STEREO* Ahead (-A) and Behind (-B). We use the time-slice approach to analyse the wave propagation and wavelet analysis to study the periodic characteristics of the wave, which will be examined in detail below.

3 RESULTS

3.1 Non-radial filament eruption

The filament eruption is presented in Fig. 1. Panel (a) provides a context view of the eruption environment in the images in AIA 193 Å. The eruption region is outlined by the box, and there is a CH in the south-west indicated by the white arrow. At the edge of this CH, the footpoint of a large loop (L1, indicated by the black arrow) can clearly be seen. Panel (b) gives a close-up of the filament before the eruption from an original 304-Å image. The filament appears as an arc. Its structure was very complex, and consisted mainly of two large strands, twisting around each other (white arrows, which can be seen better in the attached animation, 304.mpg). In addition, the movement of the filament at 193 Å was not very evident before the eruption, but some brightenings around the footpoints of the strands at 304 Å could be an indicator of the filament activation. Finally, the evolution details of the filament eruption are displayed in snapshots of AIA 193 Å (c and d). At about 15:50 UT, the filament was rising slowly. Owing to a loss of equilibrium, the northern part of the filament broke out first and rose earlier and more quickly, and the rising filament appeared to be inclining towards the south. During the gradually ascending process, the filament was heated, and the dark material became fainter (panel d). Note the angle at the north upper turning between the top and the northern part of the filament: it was clearly changed from an acute angle to an obtuse one during the eruption (panels c and d), which confirms that the filament was dragged towards the south during the ascent. At about

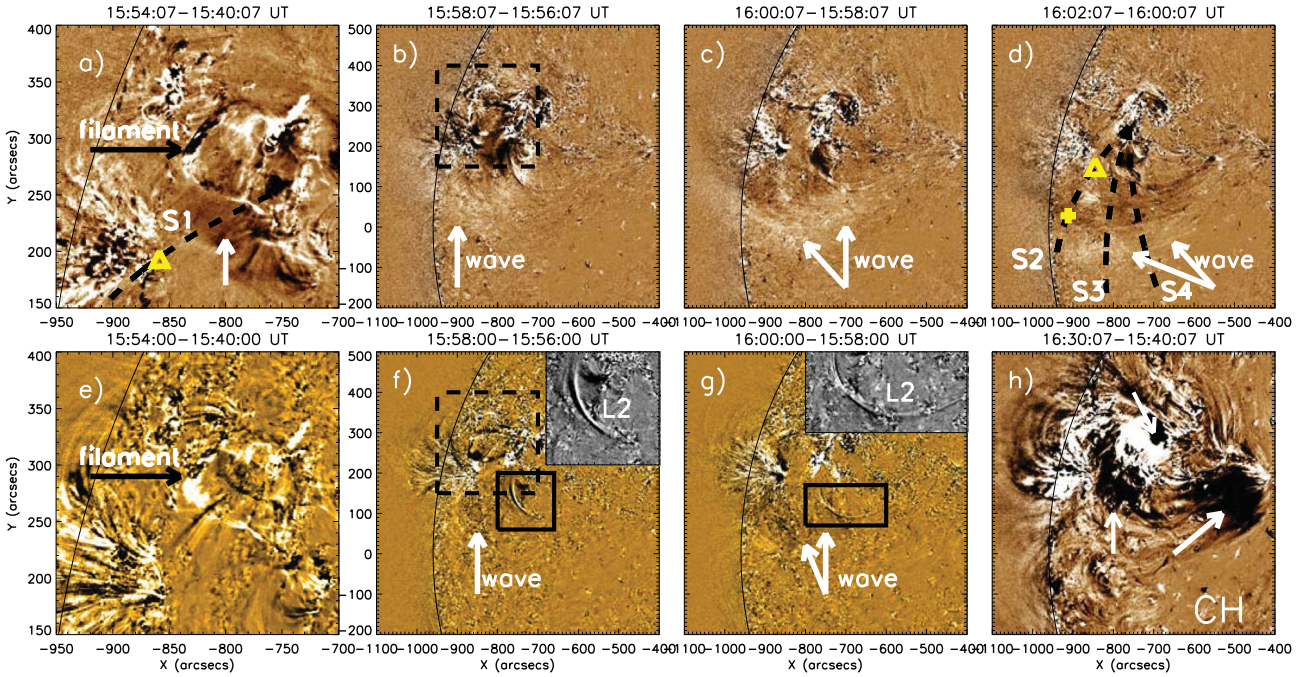

Figure 2. Coronal wave and associated features shown in AIA 193 (panels a–d and h) and 171 Å (panels e–g). The fields of view (FOVs) of panels (a) and (e) are indicated by the dashed boxes in the second column. The white arrows in panels (a) and (h) show the dimmings. The plus in panel (d) and triangles in panels (a) and (d) indicate the points used in the time-slice and wavelet analysis. The solid boxes in panels (f) and (g) represent the FOV of the upper right plots. The sectors in panels (a) and (d), S1–S4, are used to obtain the time-slice images in Fig. 3.

15:54 UT, the rising filament accelerated impulsively and erupted. It appears that the filament was rotating, and the northern part was thrown towards the south. Therefore, the erupting filament suffered an obvious non-radial motion. As a result of the filament eruption, clear ribbon-like flaring features appeared (the box in panel e), and the features spread horizontally (see 304.mpg). The light-curve of the flaring region is plotted in panel (f). The intensity increased abruptly at about 15:50 UT, close to the onset of the filament eruption (dashed line). After achieving a peak value at about 16:06 UT, the intensity slowly began to decrease. The small peak at about 15:30 UT (indicated by the arrow) confirms the filament activation.

3.2 Coronal wave

The non-radial filament eruption was associated with a coronal wave, and the evolution of the coronal wave is displayed in AIA 193 (panels a–d and h) and 171 Å (panels e–g) in Fig. 2 (better seen in the attached animation, diff193.mpg). At 15:54 UT, the erupting filament in 193 Å was more evident than that in 171 Å (black arrows in panels a and e). Dimmings appeared near the south footpoint of the filament (the white arrow in panel a), as a result of the expansion of the overlying loops driven by the erupting filament. Owing to the faintness of the wave, the running-difference images are opted to enhance the wavefront, and the wave only appears in a narrow angle extent in the south of the eruption region (arrows in panels b–d). The appearance of its propagation is likely because the wave occurred close to the solar limb. Correspondingly, the front in 171 Å appears as the emission reduction (arrows in panels f and g), which implies that the cooler material was probably heated to a higher temperature (Liu et al. 2010). During the wave propagation, a loop (L2) close to the eruption region in the south oscillated. The L2 oscillation is more obvious in 171 Å (solid boxes in panels f and g), and a close-up is displayed in the top right corners of these panels. It is evident that the oscillation also spread towards the west along L2. After the eruption (panel h), there were twin dimmings in the core region of the eruption (thin arrows), representing evacuated footpoints of the erupting flux rope. In addition to the core dimmings, there were large remote dimmings (the thick arrow) on the edge of the CH, implying the stretching of L1. Additional remote dimmings should be at another footpoint of L1 in the north-east of the eruption region and were probably covered by the intensity of neighbouring loops. The twin core-dimmings and twin remote-dimmings in the eruption is consistent with quadrupolar dimmings, first proposed by Yang et al. (2011).

In order to analyse the propagation of the wavefront, we chose four great circles (S1–S4; the dashed lines in panels Fig. 3a and d) that originate from the eruption centre ($x = -760''$, $y = 250''$). Fig. 3 displays the wave evolution in S1–S4, and the wavefronts exhibit bright inclined stripes, indicated by white arrows. The following wavespeeds and associated errors are obtained by linear fits, assuming that the measurement uncertainty of the selected points is 4 pixel (∼1.74 Mm). The selected points are marked as yellow plus signs and are connected by red dotted lines. In S1, it is difficult to identify the wave signatures from the bright coronal structures, but a sharp slower perturbation signal was identified (rightward arrows) ahead of the erupting filament (the downward arrow). The slower perturbation started at about 15:48 UT at a speed of 100 km s^{-1}. At about 15:54 UT, almost simultaneous with the onset of the filament eruption, it abruptly accelerated to 291 ± 7 km s^{-1} and vanished at the coronal brightenings (the yellow triangle, $x = -859''$, $y = 194''$, also indicated in Fig. 3a). In S2, this slower sharp perturbation (the thin black arrow) had a speed of 283 ± 7 km s^{-1} and also stopped at the brightenings (the yellow triangle, $x = -845''$, $y = 150''$, also indicated in Fig. 3d). The diffuse fast wave propagated for a long distance at a velocity of about 436 ± 11 km s^{-1}. The black box indicates the interface between the fast diffuse wave and the slower

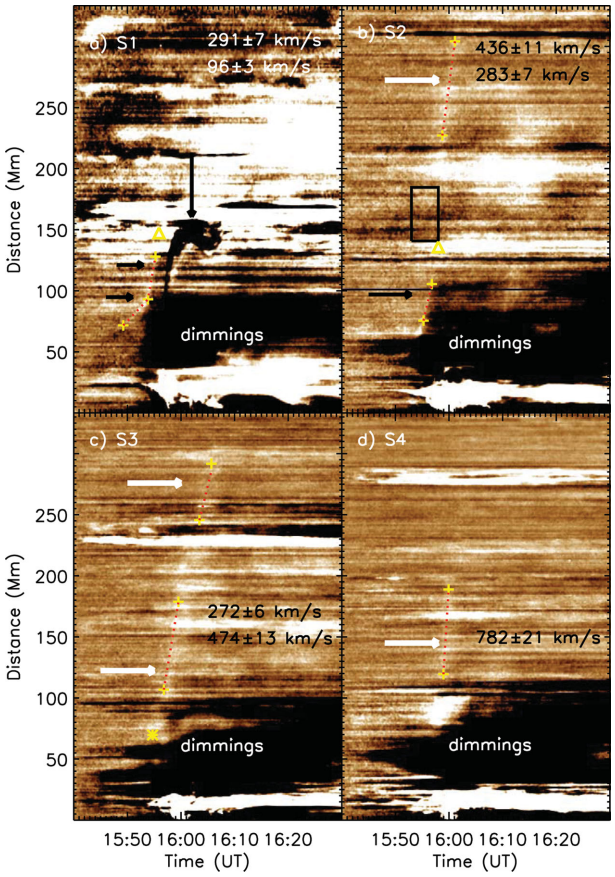

Figure 3. Base-difference time-slice images obtained from sectors S1–S4 (black dashed lines in Fig. 2) in 193 Å. Wave signatures are indicated by the white arrows, and black arrows show the erupting filament and expanding loops. The triangles in panels (a) and (b) indicate the stop location of the expanding loops, and the asterisk in panel (c) indicates the wave onset. The rectangle in panel (b) shows the space between the fast wave and the slow perturbation. Plus signs connected by dotted lines mark selected points in linear fits, shown with the fitted velocities.

sharp perturbation, which clearly shows that the two perturbations are different and clearly separated. In S3, the fast wave begins at about 15:54 UT (the yellow asterisk), nearly coincident with the onset of the filament eruption. It first propagates at a constant speed of $474 \pm 13\,\mathrm{km\,s^{-1}}$ for about 100 Mm, then decelerates to a velocity of $272 \pm 6\,\mathrm{km\,s^{-1}}$. In S4, the wave speed was about $782 \pm 21\,\mathrm{km\,s^{-1}}$, much faster than those in other directions, probably as a result of the refraction of the local coronal structures. In addition, there were clear dimmings in these directions, and the extent of the dimmings was far less than that of the coronal wave. In some non-wave theories, coronal waves are regarded as part of CME structures (i.e. expanding loops). The dimmings are disc signatures of the CME and can reflect the boundary of the associated CME. The extent of the wave is greater than that of the dimming, so it can demonstrate that the coronal wave is the true wave rather than the CME structure.

Finally, in order to identify the wave nature of the fast coronal wave, we performed a wavelet analysis of the light-curve (with the average value subtracted) of a characteristic point on S2 (the yellow plus in Fig. 2d; $x = -912''$, $y = 28''$), and the result derived from the Morlet wavelet transform method (Torrence & Compo 1998) is shown in Fig. 4. After the wave onset (the dashed line), the intensity is enhanced, and an obvious harmonic pattern appears (panel a). In panel (b), the white contours define regions where the wavelet power is significant, and they represent the real periodic signals at a confidence level of 99 per cent. The strongest signal period (the deeper colour) is approximately 650 s and is more apparent in the global spectrum (panel c). In addition, on the sides of the peak period, there are some other periods of about 1000 and 300 s, indicated by the black patches in the 99 per cent contours. The period of 1000 s nearly dominates over the full span of the observations, which can be neglected for the wave. Comparing with the wave onset (the dashed line), the strongest signal probably emerged with the filament activation, but the decrease inclination of the period is probably associated with the coronal wave. The shorter period of 300 s has a close temporal relationship with the coronal wave and lasts for nearly three cycles. The periodic characteristics of 650 and 300 s are thus closely associated. The wave analysis provides strong evidence for the periodic wave nature of the coronal wave (as argued by e.g. Ballai et al. 2005). The details of different periods will be investigated in a future work.

3.3 Coronal mass ejection

The eruption was followed by a CME, which was detected by the twin coronagraphs on *STEREO*. Owing to its being too faint in the COR1-A, the CME is shown only in composite images of the inner EUVI-B 195 Å with the outer COR1-B images in the upper panels of Fig. 5. The CME first arrived in the COR1 field of view (FOV) at about 16:15 UT. The CME had a velocity of about $300\,\mathrm{km\,s^{-1}}$, estimated by the fronts in the upper panels. It did not show the evident non-radial motion in COR1, and the appearance could also be caused by the viewing angle, namely the line-of-sight effect. The CME was also caught by the LASCO/C2 on the *SOHO* (bottom panels). The CME first entered the LASCO/C2 FOV at about 16:36 UT, and became brighter and clearer in the following images. In panel (e), the CME bright front has a central position angle (CPA) of 57° (black line), and the southern leg is at a PA of ∼110° (white line). The southern part of the CME front was brighter and stronger than the northern part, which is probably related to the non-radial filament eruption. Note that the southern part of the CME hardly expanded towards the south, as it was probably stopped by the open fields of the neighbouring CH. The linear speed of the CME in the LASCO/C2 was about $375\,\mathrm{km\,s^{-1}}$ at the measurement PA (MPA, the line in panel f) of 81° (http://cdaw.gsfc.nasa.gov/CME_list/UNIVERSAL/2011_08/univ2011_08.html). The inconsistency between the CPA and MPA also supports the non-radial movement of the CME. The CPA is usually equal to the position angle connecting the eruption source region and the disc centre for the radial CME. The MPA is the selected angle used to determine the CME speed in the fastest direction. For a non-radial expansion, the CME propagates in an angle extent, but the fastest propagation angle is not the CPA. So, the MPA is different from the CPA in non-radial events.

4 DISCUSSION AND CONCLUSIONS

Using observations in the line-of-sight magnetic field, EUV and white light from the HMI, AIA, EUVI, COR1 and LASCO/C2, we present a coronal wave associated with a filament eruption on 2011 August 10. Owing to the magnetic activity in the source region, the filament experienced an extended activation followed by an abrupt ejection. During the eruption, the filament rotated and finally moved out non-radially as well as the subsequent CME, and there formed an associated coronal wave.

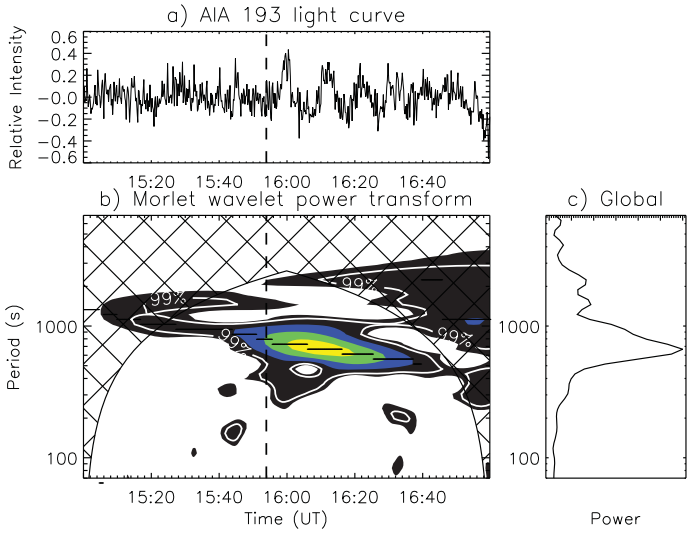

Figure 4. (a) The intensity variance of the plus characteristic point on S2, and (b, c) the power spectrum of the intensity. Deeper colours correspond to higher wavelet power, and the dashed lines indicate the wave onset.

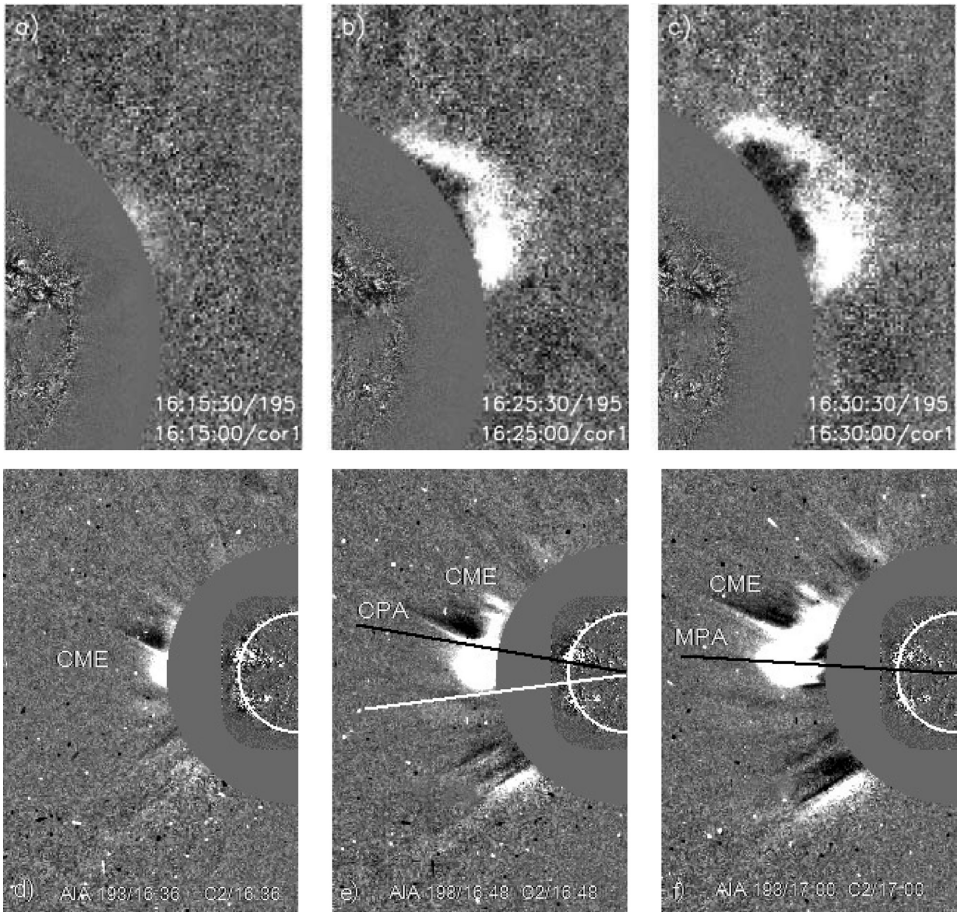

Figure 5. Composite inner EUVI-B 195-Å and outer COR1-B images (upper panels), and composite inner AIA 193-Å and outer LASCO/C2 images (bottom panels), showing the movement of the non-radial coronal mass ejection (CME). The white line indicates the position angle of the southern leg of the CME.

Intriguingly, the eruption was closely associated with a fast wave and a slower perturbation. We now discuss whether the findings are similar to those of Chen & Wu (2011), who found fast and slow waves with the *SDO* data and confirmed the model of Chen et al. (2002). On one hand, the slow perturbation first underwent slow propagation before the filament eruption, then suddenly accelerated almost simultaneously with the filament eruption, and was eventually stopped by the coronal brighenings (indicated by the triangles in Figs 2 and 3). On the other hand, the slower perturbation only appeared in a limited direction. The velocity of the fast wave is in

the range 430–480 km s^{-1}, and that of the slower perturbation is about 300 km s^{-1}. Chen et al. (2002) predicted that the speed of the fast wave should be about three times that of the slow wave in their model. As to the three-times relationship between the velocities of the fast wave and slower perturbation, it is changed significantly, not slightly, in our event. Therefore the wave studied here cannot be accounted for by this model. Moreover, the speed of the slower perturbation is approximately equal to that of the CME. Therefore, the slower perturbation is probably an indicator of the expanding loop enveloping the erupting filament, not the true wave signature. Hence, the observed structures of the fast wave and slower perturbation are different from those of Chen & Wu (2011). The slower perturbation is the expanding loop, which should exist in most eruptions, and the fast coronal wave is the true wave. In addition, loop oscillations and deceleration occurred concurrently along some directions of wave propagation. It is plausible that the fast coronal wave was a fast-mode MHD wave that was probably triggered by the rapid expansion of the overlying loop of the erupting filament, owing to the close spatial and temporal relationship.

Moreover, it is very interesting that the wave speed in S4 is higher than that in other directions. We cannot give a reliable interpretation of this high speed until more detailed observations become available. The nature and origin of EUV waves remain subtle, necessitating further observations and theoretical work.

ACKNOWLEDGEMENTS

The authors are grateful to the anonymous referee, and thank the *SDO* team, the *STEREO* group and the *SOHO* consortium for providing the data. We are also grateful to the CME catalog. This CME catalog is generated and maintained at the CDAW Data Center by NASA and the Catholic University of America in cooperation with the Naval Research Laboratory. This work was supported by the 973 Program 2011CB811403, by the Yunnan Province Natural Science Foundation (NSF) 2013FB085, and by the Natural Science Foundation of China under grants 10973038, 11173058 and 11103090. RZ and RE thank the UK Science and Technology Facilities Council for the support they received. RE is also grateful to Natural Science Foundation, Hungary (OTKA, ref. no. K83133) and acknowledges M. Kéray for patient encouragement.

REFERENCES

Attrill G. D. R., Harra L. K., van Driel-Gesztelyi L., Démoulin P., 2007, ApJ, 656, L101
Ballai I., Erdélyi R., Pintér B., 2005, ApJ, 633, L145
Bemporad A., Mierla M., Tripathi D., 2011, A&A, 531, A147
Biesecker D. A., Myers D. C., Thompson B. J., Hammer D. M., Vourlidas A., 2002, ApJ, 569, 1009
Brueckner G. E. et al., 1995, Sol. Phys., 162, 357
Chen P., 2006, ApJ, 641, L153
Chen P., Wu Y., 2011, ApJ, 732, L20
Chen P., Wu S., Shibata K., Fang C., 2002, ApJ, 572, L99
Cheng X., Zhang J., Olmedo O., Vourlidas A., Ding M. D., Liu Y., 2012, ApJ, 745, L5
Cliver E. W., Laurenza M., Storini M., Thompson B. J., 2005, ApJ, 631, 604
Cohen O., Attrill G. D. R., Manchester W. B., IV, Wills-Davey M. J., 2009, ApJ, 705, 587
Delaboudinière J. P. et al., 1995, Sol. Phys., 162, 291
Delannée C., Török T., Aulanier G., Hochedez J. F., 2008, Sol. Phys., 247, 123
Downs C., Roussev I. I., van der Holst B., Lugaz N., Sokolov I. V., Gombosi T. I., 2011, ApJ, 728, 2
Gallagher P. T., Long D. M., 2011, Space Sci. Rev., 158, 365
Gopalswamy N. et al., 2009, ApJ, 691, L123
Green L. M., Kliem B., Török T., van Driel-Gesztelyi L., Attrill G. D. R., 2007, Sol. Phys., 246, 365
Howard R. A. et al., 2008, Space Sci. Rev., 136, 67
Ji H., Wang H., Schmahl E. J., Moon Y.-J., Jiang Y., 2003, ApJ, 595, L135
Kaiser M. L., Kucera T. A., Davila J. M., St. Cyr O. C., Guhathakurta M., Christian E., 2008, Space Sci. Rev., 136, 5
Koleva K., Madjarska M. S., Duchlev P., Schrijver C. J., Vial J.-C., Buchlin E., Dechev M., 2012, A&A, 540, A127
Lemen J. R., Title A. M., Akin D. J., Boerner P. F., Chou C., Drake J. F., Duncan D. W., Edwards C. G., 2012, Sol. Phys., 275, 17
Li T., Zhang J., Yang S., Liu W., 2012, ApJ, 746, 13
Liu R., Liu C., Wang S., Deng N., Wang H. M., 2010, ApJ, 725, L84
Long D. M., Gallagher P. T., McAteer R. T. J., Bloomfield D. S., 2008, ApJ, 680, L81
Moreton G. E., 1960, AJ, 65, 494
Moses D. et al., 1997, Sol. Phys., 175, 571
Ofman L., Thompson B. J., 2002, ApJ, 574, 440
Olmedo O., Vourlidas A., Zhang J., Cheng X., 2012, ApJ, 756, 143
Patsourakos S., Vourlidas A., 2012, Sol. Phys., 281, 187
Pesnell W. D., Thompson B. T., Chamberlin P. C., 2012, Sol. Phys., 275, 3
Schmieder B., Démoulin P., Aulannier G., 2013, Adv. Space Res., 51, 1967
Sterling A. C., Moore R. L., 2004, ApJ, 602, 1024
Thompson B. J., Myers D. C., 2009, ApJS, 183, 225
Thompson B. J., Plunkett S. P., Gurman J. B., Newmark J. S., St. Cyr O. C., Michels D. J., 1998, Geophys. Res. Lett., 25, 2465
Thompson B. J., Gurman J. B., Neupert W. M., Newmark J. S., Delaboudinière J.-P., St. Cyr O. C., Stezelberger S., Dere K. P., 1999, ApJ, 517, L151
Thompson W. T., Kliem B., Török T., 2012, Sol. Phys., 276, 241
Torrence C., Compo G. P., 1998, Bull. Am. Meteorol. Soc., 79, 61
Veronig A. M., Muhr N., Kienreich I. W., Temmer M., Vršnak B., 2010, ApJ, 716, L157
Wang Y. M., 2000, ApJ, 543, L89
Wang H., Shen C., Lin J., 2009, ApJ, 700, 1716
Warmuth A., 2010, Adv. Space Res., 45, 527
Wills-Davey M. J., Attrill G. D. R., 2009, Space Sci. Rev., 149, 325
Wills-Davey M. J., DeForest C. E., Stenflo J. O., 2007, ApJ, 664, 556
Wu S. T., Zheng H. N., Wang S., Thompson B. J., Plunkett S. P., Zhao X. P., Dryer M., 2001, J. Geophys. Res., 106, 25089
Yan X. L., Pan G. M., Liu J. H., Qu Z. Q., Xue Z. K., Deng L. H., Ma L., Kong D. F., 2013, ApJ, 145, 153
Yang J., Jiang Y., Zheng R., Hong J., Bi Y., Yang L., 2011, Sol. Phys., 270, 551
Zhang J., Liu Y., 2011, ApJ, 741, L7
Zheng R., Jiang Y., Hong J., Yang J., Bi Y., Yang L., Yang D., 2011, ApJ, 739, L39
Zheng R., Jiang Y., Yang J., Bi Yi, Hong J., Yang B., Yang D., 2012, ApJ, 747, 67
Zhukov A. N., 2011, J. Atmos. Sol. Terr. Phys., 73, 1096
Zhukov A. N., Auchère F., 2004, ApJ, 427, 705

SUPPORTING INFORMATION

Additional Supporting Information may be found in the online version of this article:

Movie 1. diff193.mpg
Movie 2. 304.mpg
(http://mnras.oxfordjournals.org/lookup/suppl/doi:10.1093/mnras/stu1361/-/DC1).

Please note: Oxford University Press are not responsible for the content or functionality of any supporting materials supplied by the authors. Any queries (other than missing material) should be directed to the corresponding author for the article.

This paper has been typeset from a TEX/LATEX file prepared by the author.